# Optical Properties of Rodlike Metallic Nanostructures: Insight from Theory and Experiment

**Jinsong Duan,[†,‡] Kyoungweon Park,[†,§] Robert I. MacCuspie,[†,∥] Richard A. Vaia,[†] and Ruth Pachter*[,†]**

*Air Force Research Laboratory, Wright-Patterson Air Force Base, Ohio 45433, General Dynamics Information Technology, Dayton, Ohio 45431, National Research Council, Washington, DC 20001, and National Institute of Standards and Technology, Gaithersburg, Maryland 20899-8520*

*Received: March 18, 2009; Revised Manuscript Received: July 13, 2009*

In this work, we combined synthesis of Au nanorods (AuNRs) and Au−Ag core−shell nanorod-like structures, of narrow size distribution in all dimensions and for a broad range of aspect ratios, with computational prediction of the localized surface plasmon resonance (LSPRs), in order to gain a better understanding of the optical response. Self-assembled AuNRs were also synthesized and characterized experimentally and theoretically. In addition, an understanding of the growth of Au−Ag core−shell nanorod-like structures for varying geometries, dielectric environments, and compositions was obtained. Controlled and precise synthesis, even for AuNRs with large aspect ratios, for Au−Ag core−shell nanostructures and AuNR pairs, enabled validation of the computational results, and development of structure−property relationships. These will, in turn, assist in the experimental characterization of AuNRs and related core−shell nanostructures.

## Introduction

Noble metal nanoparticles, specifically gold nanorods (AuNRs), are useful for a broad range of applications, for example, as potential cancer diagnostic markers,[1] as based on the localized surface plasmon resonance (LSPR).[2,3] Notably, AuNRs were shown to demonstrate stronger molecular adsorption as compared to spherical nanoparticles, a large surface electromagnetic field, and of course the ability to form field aggregates. Recently, Murphy et al.[4] reviewed the utility of metal NRs, for example, showing improved sensitivity of the longitudinal LSPRs of AuNRs to changes in the refractive index of the dielectric environment, which can be exploited as a tool to confirm surface modification by polymers and biomolecules, increased surface-enhanced Raman scattering (SERS), as compared to spheres, and in self-assembled monolayer sandwich geometries. Interestingly, AuNRs also show significant reduction in the plasmon dephasing as compared to spheres.[5] Furthermore, metallic NRs were conceived as building blocks in antennas,[6,7] while a metal nanowire composite, constructed from parallel pairs of silver nanowires, was suggested to exhibit negative magnetic permeability and dielectric permittivity in the visible and near-infrared spectral ranges.[8] Coupling between molecular and plasmonic resonances in freestanding dye−gold NR hybrid structures was recently observed.[9] In addition, multifunctional or core−shell NRs, which vary not only in geometry but also in composition, demonstrated possible utility for a wide range of biomedical applications.[10] Au−Ag core−shell NRs were used as a platform for multiple aptamer immobilizations, shown to be highly promising for cancer cell targeting,[11] while selective detection of iron ions was demonstrated with core−shell nanostructures.[12]

The promise of AuNR applications led to a surge of synthetic work, in examining self-assembly,[13,14] the role of the surfactant in seed-mediated synthesis,[15] effects of various parameters on structural evolution,[16] and in tuning the SERS response.[17] Synthesis of core−shell[18] and spherical[19] nanostructures was thoroughly reviewed,[20] including controlled growth,[21] and the optimization of parameters that affect growth.[22,23] Recently, a critical survey of various methods for the shape- and size-selective synthesis of anisotropic metallic nanostructures was summarized.[24]

At the same time, numerical methods for solving Maxwell's equations for particles of arbitrary shape and composition, beyond Mie's analytical theory, have been applied. Methods include, among others, the finite difference time domain (FDTD),[25] the boundary element method (BEM),[26] and the discrete dipole approximation (DDA), where an array of polarizable dipolar elements that comprise the shape of the metal nanoparticle is used, providing the response to an incident electric field. Application of DDA to this problem was introduced by Schatz and co-workers[27] and proven to be particularly successful because of its ability to predict the optical extinction of particles of varying shape and composition.[28–34] However, although synthetic and computational studies are abundant, a careful and systematic comparison of experimentally characterized nanoparticles with computational prediction, particularly for more complex nanostructures, is still lacking.

In this work, we combined synthesis of AuNRs and Au−Ag core−shell NRs of narrow size distribution in all dimensions and for a broad range of NR aspect ratios, with theoretical prediction, in order to gain an understanding of the optical response to the material's structure and properties. Self-assembled NRs were also synthesized and characterized experimentally and computationally to expand the range of materials studied. Further, an understanding of the growth of Au−Ag core−shell NR-like structures for varying dielectric environments and compositions was obtained, as a result of pairing computational prediction with experimental data. This

* To whom correspondence should be addressed. E-mail: ruth.pachter@wpafb.af.mil.
[†] Wright-Patterson Air Force Base.
[‡] General Dynamics Information Technology.
[§] National Research Council.
[∥] National Institute of Standards and Technology.

10.1021/jp902448f CCC: $40.75 
Published on Web 08/11/2009

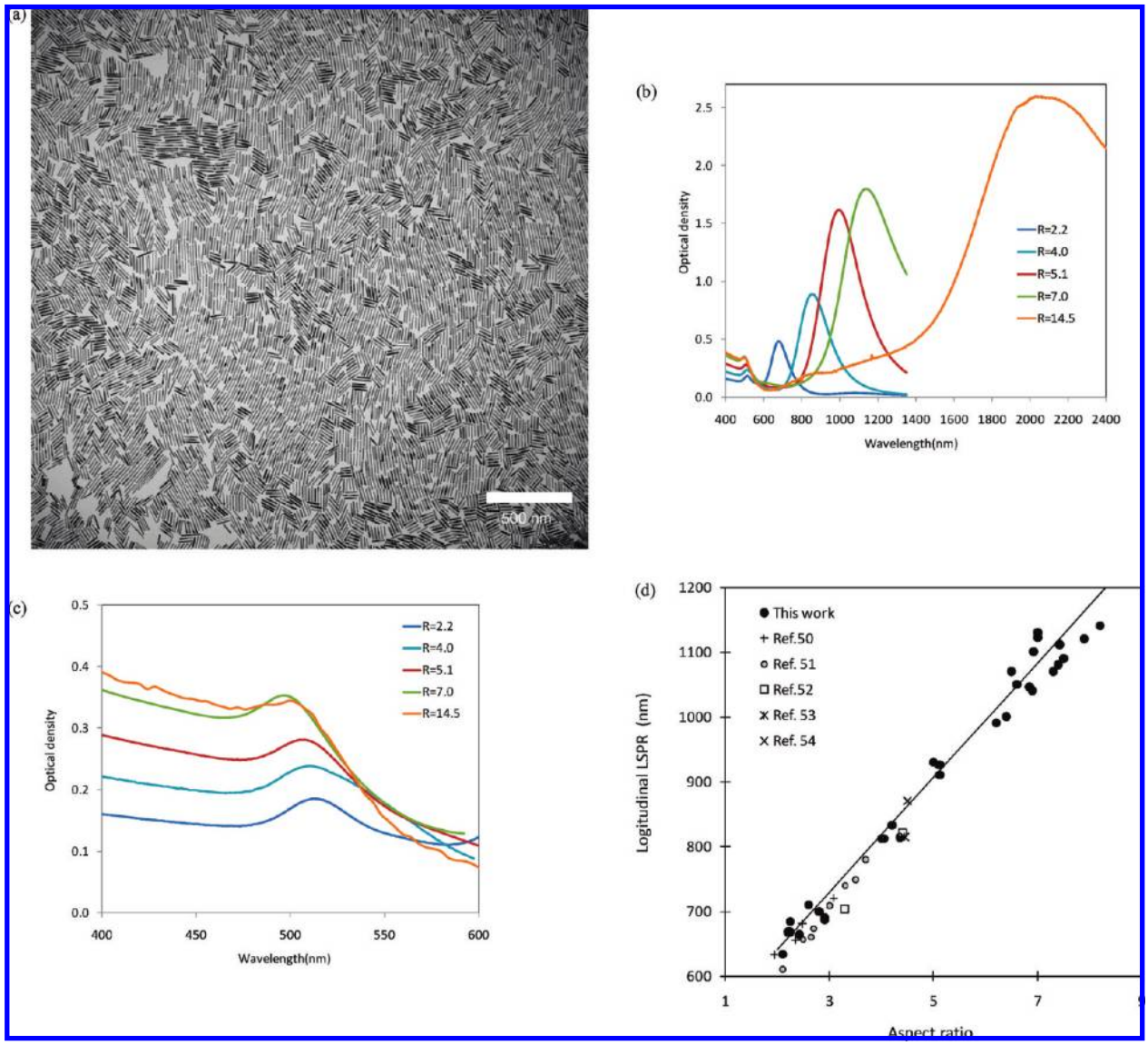


**Figure 1.** (a) TEM image of AuNRs used in the size measurement. This specific sample of AuNRs has the following dimensions: $L = 68.8 \pm 11.7$ nm and $D = 13.6 \pm 1.5$ nm. Experimental spectra of (b) longitudinal and (c) transverse LSPRs for AuNRs with various aspect ratios (dimensions summarized in Table 1S, Supporting Information); (d) comparison of experimentally measured longitudinal LSPRs by various groups.

is the first stage in our effort to engineer plasmonic nanostructures, e.g., for enhancement of molecular fluorescence, where the LSPR has to be tuned.[35]

## Methods

**Computational.** All calculations were carried out applying the DDA, coded in freely available DDSCAT.[36] The theory of the DDA for an array of dipoles, introduced by Purcell and Pennypacker,[37] further developed by Draine et al.,[38] is discussed elsewhere.[39] A comparison between DDA implementations[40] and an extension of the approach to larger systems, in the order of $10-20\ \lambda$, such as for biological systems, was also reported.[41] Previously, DDA calculations were compared to FDTD,[42] showing good agreement, and the performance of FDTD, BEM, and DDA was recently assessed.[43]

Note that within FDTD, the propagation of the electromagnetic field is defined on a spatial grid through consecutive time steps, so that the whole spectrum can be obtained from a single computational run. However, appropriate treatment of boundary conditions has to be applied, and description of complex geometries and dispersive materials has to be specifically taken into account. On the other hand, DDA, in which the response to the electric field is calculated in the frequency domain, is advantageous because it can readily be applied to the calculation of scattering and absorption for inhomogeneous and anisotropic nanoparticles. Specifically, the parameters of the scattering problem, namely shape, size, and orientation relative to the applied field in the laboratory frame, are provided as input for the calculation within the DDA method. This is especially important for modeling core−shell structures because of the complex geometries. In addition, the tabulated dielectric function of the nanoparticle, dependent on its composition, as a function of wavelength, for each metal, was provided. The electric field was assumed to be either parallel (exciting the longitudinal LSPR), or perpendicular to the major axis of the NR (exciting the transverse LSPR). Bulk and thin film dielectric functions were used. Calculations were performed for cylinders of length $L$ and diameter $D$ (aspect ratio $R = L/D$), capped by hemispheres, and an aqueous medium assumed ($n = 1.33$).

**Experimental.**[44] ***Synthesis of AuNRs.*** Commercial cetyltrimethylammonium bromide (CTAB) and benzyldimethylhexadecylammonium chloride (BDAC) were purchased from TCI

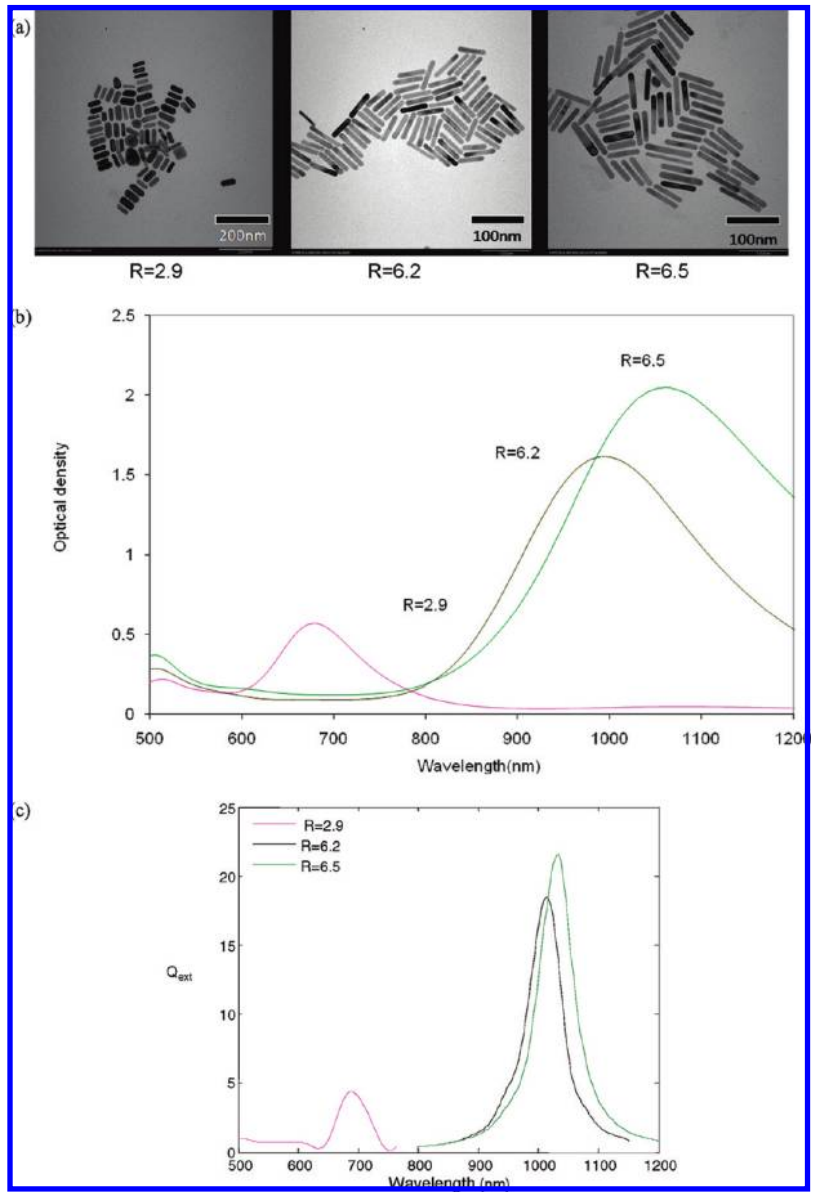


**Figure 2.** (a) TEM images of AuNRs of different aspect ratios; (b) experimental longitudinal LSPRs for AuNRs shown in (a) with the geometrical parameters $L$, $D$: 54.8 ± 7.1 nm, 20.1 ± 5.1 nm; 65.7 ± 8.0 nm, 10.6 ± 1.7 nm; 78.8 ± 15.2 nm, 12.5 ± 4.3 nm, respectively; (c) calculated longitudinal LSPR results.

America (Portland, OR). $HAuCl_4$, $AgNO_3$, sodium borohydride and L-ascorbic acid were purchased from Aldrich (St. Louis, MO). All chemicals were used as received without further purification. The synthesis followed the seed-mediated growth method previously outlined by Nikoobakht et al.[45] Briefly, the seed solution was freshly prepared by adding ice-cold $NaBH_4$ solution (0.6 mL, 0.01 mol·$L^{-1}$) into a solution composed of a mixture of $HAuCl_4$ (0.025 mL, 0.1 mol·$L^{-1}$) and CTAB (10 mL, 0.1 mol·$L^{-1}$). The growth solution was prepared separately by mixing the aqueous solution of $HAuCl_4$ (0.5 mL, 0.1 mol·$L^{-1}$), $AgNO_3$ (0.08 mL, 0.1 mol·$L^{-1}$), CTAB (50 mL, 0.2 mol·$L^{-1}$), and BDAC (50 mL, various concentrations range from 0.02 to 0.25 mol·$L^{-1}$) at room temperature. Next, ascorbic acid (0.55 mL, 0.1 mol·$L^{-1}$) was added to the growth solution as a mild reducing agent; then, the seed solution (0.1 mL) was added to the growth solution, where the color of the growth solution was observed to be slowly changing from clear to violet, indicating growth of AuNRs.

The as-made solution contains AuNRs with less than 20% of spherical particles. The spherical particles were removed by carefully controlled centrifugation.[46] The as-made AuNR solution was centrifuged at 5600$g$ for 40 min by using Allegra X-22 centrifuge (Beckman Coulter, Fullerton, CA). After the centrifugation, the tube was visibly inspected. The concentrated dark solution at the bottom of the tube which contains most of spherical particles was removed by using a syringe. The supernatant was carefully removed. The solidlike deposit on the side wall which contains AuNRs was dissolved in distilled water. The typical dimensions of the AuNRs, expressed in terms of the aspect ratio $R$, ranged from 3 to 10, with $L$ from 30 to 150 nm, and $D$ from 8 to 20 nm. The size and $R$ of the AuNRs were controlled by changing the concentration and mixing ratio of surfactants. AuNRs with $R > 13$ were obtained when $AgNO_3$ was not added in the growth solution. The as-made solution contains less than 20% of AuNRs. AuNRs were purified by controlled centrifugation. The resulting AuNRs usually have more size polydispersity than those obtained by adding $AgNO_3$.

***Secondary Growth of AuNRs.*** Additional $HAuCl_4$ (0.01 mL, 0.1 mol·$L^{-1}$) and ascorbic acid (0.1 mol·$L^{-1}$) at a specific molar ratio were added to 5 mL of purified AuNR template solution.

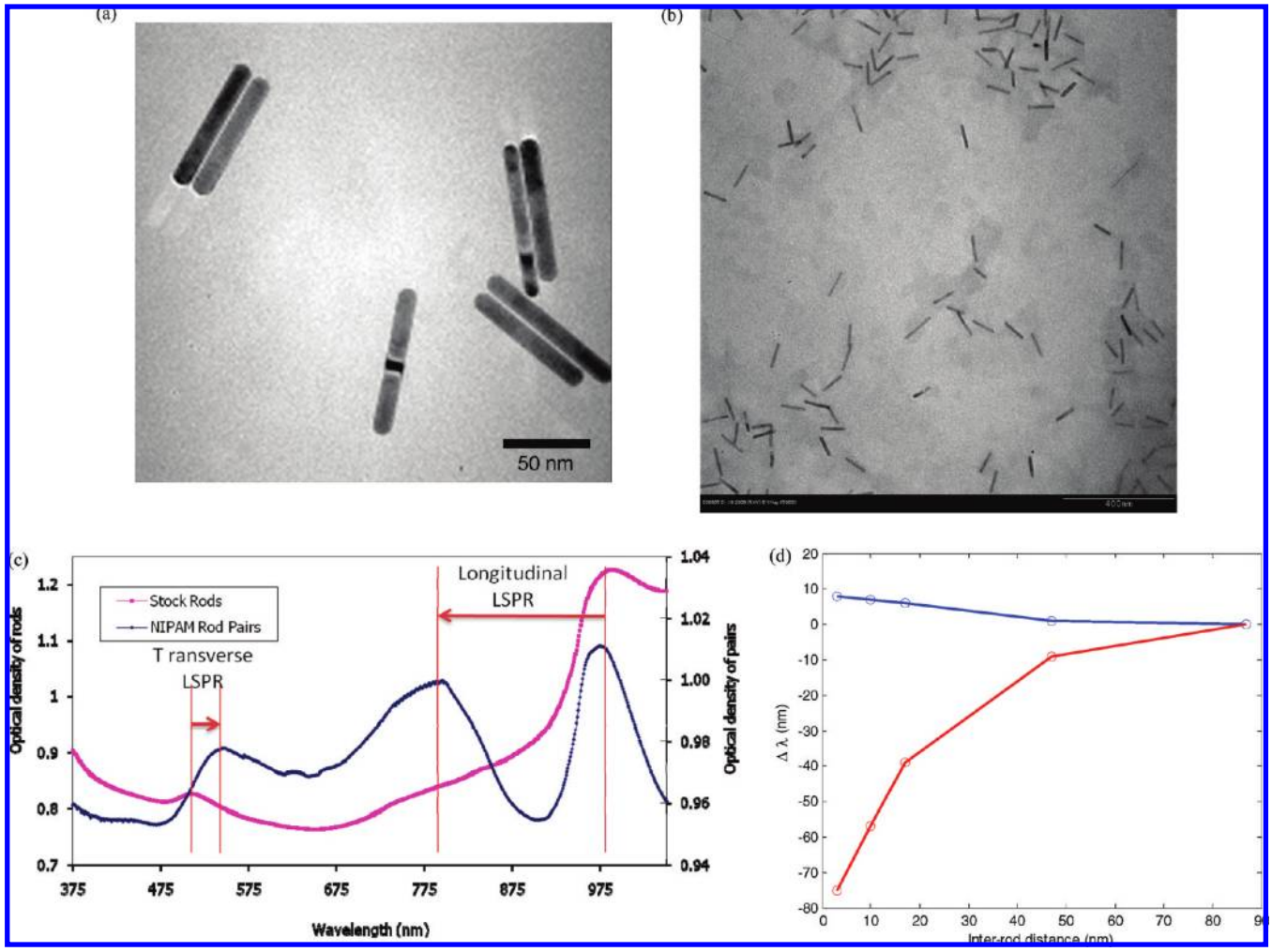


**Figure 3.** TEM images of (a) unreacted AuNRs mixed with AuNR pairs, as compared to a solution of (b) single NRs (NIPAM, *N*-isopropylacrylamide); (c) corresponding longitudinal and transverse experimental spectra; (d) calculated shifts of side-by-side AuNRs as a function of inter-rod distance: red, longitudinal; blue, transverse LSPRs.

***Deposition of Silver on Gold Core NRs.*** Additional $HAuCl_4$ (0.01 mL, 0.1 mol·$L^{-1}$), $AgNO_3$ (0.03 mL, 0.1 mol·$L^{-1}$), and ascorbic acid (0.02 mL, 0.1 mol·$L^{-1}$) were added to 5 mL of a purified AuNR template solution. The location of Ag deposition (as a tip or as a shell) was controlled by adjusting the pH, ranging from 3 to 11, by adding NaOH.

***Synthesis of AuNR Pairs by Ion-Exchange Resin Surface Masking and Layer-by-Layer Buildup.*** AuNRs were allowed to incubate on a DOWEX 50W-X8 strong cation-exchange resin (Aldrich, St. Louis, MO) for 24 h. The resulting supernatant was removed, and the resin was washed three times with distilled water. Next, a thiol-linker molecule, such as 1,6-hexanedithiol or 3-mercaptopropionic acid, was allowed to react onto the exposed Au surface for 1 h. A stochiometry of 10:1 for thiol molecules to available Au binding sites was evaluated, which was based on the exposed surface area of Au on the AuNRs, the number of Au atoms per unit surface area based on the van der Waals diameter, and the binding ratio of 1.8 Au per thiol molecule, as observed for thiol−Au self-assembled monolayers.[47] The resin was then washed with distilled water once. The second layer of AuNRs was then deposited. For dithiol linkers, neat AuNRs were deposited directly. For linkers with $\omega$-carboxyl groups, 300 mL of 2.5 nmol·$L^{-1}$ AuNRs functionalized with cystamine were added to the resin with a fresh solution of 0.100 mL of 10 mmol·$L^{-1}$ *N*-hydroxysuccinimide (NHS), 0.100 mL of 75 mmol·$L^{-1}$ *N*-(3-dimethylaminopropyl)-*N*′-ethylcarbodiimide hydrochloride (EDC), and 1.500 mL of distilled water. The solutions were allowed to react for 1 h at room temperature before the reaction supernatant was removed, and the resin then washed three times with distilled water. Subsequently, 2.0 mL of a 0.1 mol·$L^{-1}$ CTAB surfactant solution was added to the resin and the resulting suspension sonicated for 10 min in a bath sonicator to release AuNRs from the resin. The resulting AuNR solution was then collected.

***Characterization.*** UV−Vis−NIR spectra were acquired with a Cary 5000 UV−vis−NIR spectrophotometer. Morphology and the mean size of AuNRs were examined by TEM (Philips CM200 LaB6 at 200 kV). For each sample, the size of more than 300 particles was measured to obtain the average size and size distribution, reported as plus or minus one standard deviation. Note that detailed characterization of Ag tipped AuNRs and Au−Ag core−shell NRs, including HRTEM and SAED, was previously reported.[23]

## Results and Discussion

**AuNRs.** Figure 1a shows a TEM of synthesized AuNRs, demonstrating that the solutions obtained contained very few spherical particles, thereby enabling better comparison with computational results. Experimental spectra are summarized in Figure 1b−c, and corresponding calculated $\lambda_{max}$ for the series of AuNRs with varying *R* are reported in Table 1S (Supporting Information). A linear relationship between the longitudinal

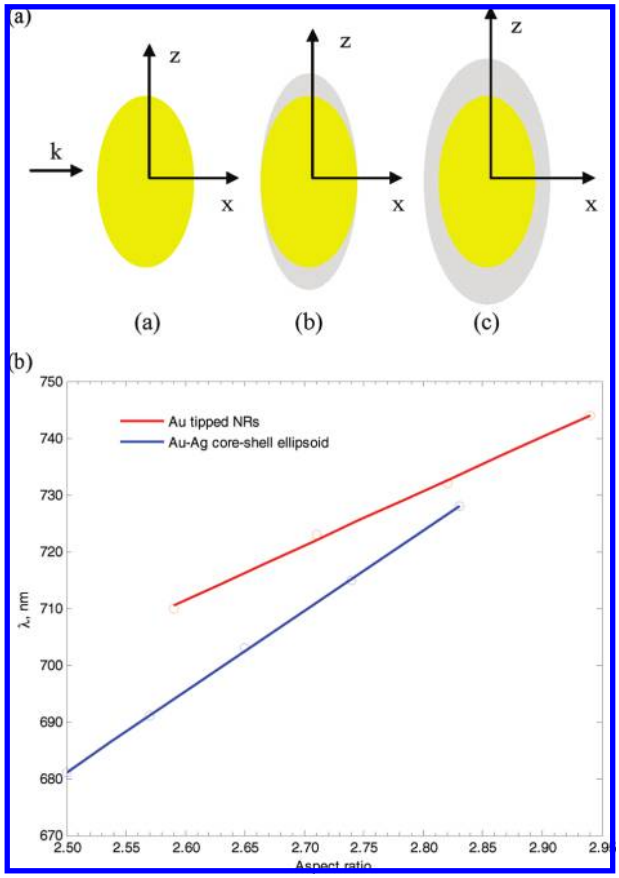


**Figure 4.** (a) (a,a) Au spheroid, (a,b) Au−Ag core−shell structure that consists of an Au spheroid with the coating built up at the ends, (a,c) thicker full coverage; (b) longitudinal $\lambda_{max}$ vs aspect ratio for nanostructures (a,b) and (a,c). Dimensions are discussed in the text.

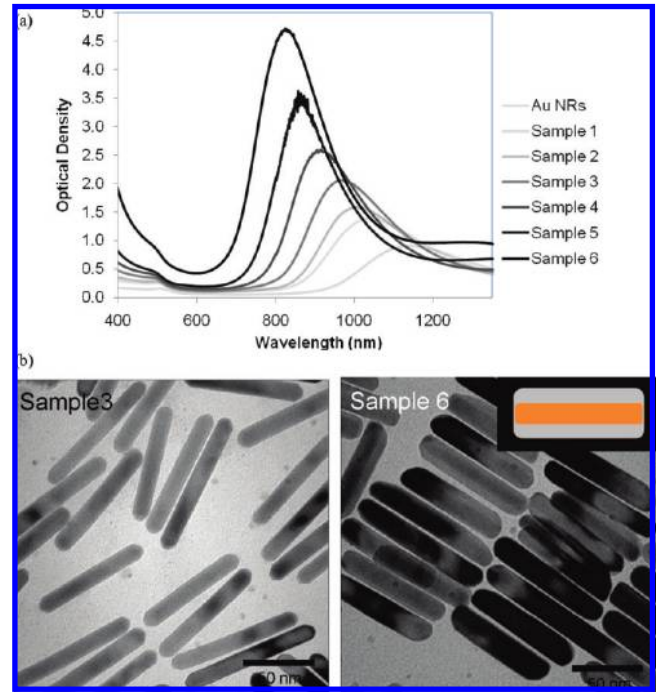


**Figure 5.** (a) Spectra of Au−Ag core−shell structures, with the dimensions summarized in Table 1; (b) TEM images of Au−Ag core−shell structures corresponding to samples 3 and 6. Inset of sample 6 shows the model geometry based on experimental characterization.

LSPR and $R$ was obtained, $\lambda_{max}(\text{exp}) = 464.0(\pm 22.2) + 88.6(\pm 6.3)R$, based on experimentally characterized values, for which five different series of AuNR with varying $R$s, were included. Note that when the imaginary part of the dielectric function is relatively small, the monotonically decreasing real part of the dielectric function determines the resonance wavelength, hence a linear relationship with $R$.[6,48–50]

The values of previously reported $\lambda_{max}$ for AuNRs[50−54] are plotted in Figure 1d along with this work's experimental data and empirical equation. Compared to previously reported results, our data confirms the linear relationship between $\lambda_{max}$ and $R$, not only in the visible wavelengths, but also in the near-infrared region. In general though, experimental $\lambda_{max}$ exhibit varying degrees of variation from the linear relation. For example, Liu et al.[53] reported $\lambda_{max}$ of about 821 and 704 nm for synthesized AuNRs having $R$s of 4.4 and 3.3, respectively, in aqueous solution. The linear regression resulted in red-shifted values for $R = 4.4$, 3.3, of 854 nm, 756 nm, respectively, which could be attributed to a mixture of AuNR geometries in the work of Liu et al. (Figure 2d in ref 53). An even larger variation was observed in comparison with the value of 814 nm reported by Ah et al.,[54] where we predicted a value of 858 nm for $R = 4.45$. A measured value of 702 nm was previously reported[13] for $R = 3.9$, while we predicted $\lambda_{max}$ of 809 nm, based on our experimental relationship. On the other hand, a better agreement was obtained for AuNRs with $R$ of 4.5,[55] where $\lambda_{max}$ of about 870 nm was reported, as compared to the experimentally derived relationship value of 862 nm reported in this work.

The differences observed in reported values for various experimental studies motivated the use of numerical predictions. Calculated $\lambda_{max}$ (Table 1S, Supporting Information) reproduced the measured transverse LSPRs, showing a small blue-shift as is expected. Somewhat larger errors were observed for the longitudinal LSPRs, which could be due to a percentage in the mixture of AuNRs with a different geometry than a cylinder capped by hemispheres. Consequently, an overall inaccurate estimation of the input geometry could result, in addition to the uncertainty in characterizing experimentally the AuNR dimensions. Interestingly, the longitudinal LSPR for an AuNR (dimensions of $L = 61.2 \pm 6.7$ nm; $D = 14.3 \pm 1.7$ nm) of about 850 nm, as reported by Xiang et al.,[22] agrees well with a value of 859 nm predicted by the linear relationship based on our DDA calculations. Previous calculations using the FDTD method for a similar geometry resulted in $\lambda_{max}$ of 742, 810, and 879 nm, for $R = 3.4$, 4.1, and 4.8, respectively, consistent with our DDA results, where we predicted, for example, $\lambda_{max}$ of 826 nm for an aspect ratio of 4.1.

The results are explained by depolarization factors, which can be derived, for example, from the analytical expression of the dipolar polarizability for a small ellipsoid, as recently reviewed.[32] As the nanoparticle becomes more elongated along the principal long axis, the depolarization factor decreases and the longitudinal resonance requires larger values of $-\text{Re}\{\varepsilon\}$, which occurs at longer wavelengths. Note that in the case of ellipsoids of revolution, the depolarization is dependent on the aspect ratio $R_3/R_1$ (where $R_1 = R_2$; $R_j$ are the half axes for an ellipsoid, and $j = 1, 2, 3$ denote the principal axes of the ellipsoid). Depolarization factors for ellipsoidal nanoparticles, in different media, including prolate spheroids, were reported.[31]

The experimental results demonstrated the importance of physical characterization of AuNR size and size distribution by standard or consensus methods[56] to achieve accurate computational prediction. To probe these relationships more closely, experimental samples of AuNRs with $R = 2.9$, 6.2, and 6.5 were carefully characterized (samples 1−3 in Figure 2).

**TABLE 1: Experimental $\lambda_{max}$ for Core−Shell Au−Ag NRs**

| | concentration of $AgNO_3$(mol·$L^{-1}$) | volume (mL) | measured thickness of shell (nm) | measured $R$ | measured $L$; $D$ (nm) | $\lambda_{max}$ (exptl) (nm) |
|---|---|---|---|---|---|---|
| AuNR | | | | $8.0 \pm 2.7$ | $88.1 \pm 23.0$; $11.2 \pm 1.8$ | 1130 |
| sample 1 | 0.2 | 5 | N/A | N/A | N/A | 1040 |
| sample 2 | 0.2 | 10 | N/A | N/A | N/A | 1007 |
| sample 3 | 0.2 | 15 | N/A | N/A | N/A | 965 |
| sample 4 | 0.2 | 20 | $2.1 \pm 1.0$ | $6.1 \pm 1.6$ | $88.1 \pm 23.0$; $15.4 \pm 3.8$ | 925 |
| sample 5 | 0.2 | 40 | $3.8 \pm 1.1$ | $5.5 \pm 1.8$ | $88.1 \pm 23.0$; $18.8 \pm 3.9$ | 860 |
| sample 6 | 0.2 | 90 | $4.8 \pm 1.1$ | $3.8 \pm 0.7$ | $88.1 \pm 23.0$; $20.8 \pm 3.9$ | 820 |

Computationally, we examined the effect of the number of dipoles used, where for sample 1, using a large number of dipoles (412 120), a good agreement with experiment was obtained, predicting a value of $\lambda_{max}$ of 690 nm, as compared to the experimental value of 680 nm. This result was improved upon by applying the dielectric function of Johnson and Christy (JC),[57] characterized for thin films. Using a larger number of dipoles in the calculation improves the accuracy by a few nanometers when comparing results for samples 2 and 3. For example, for $R = 6.5$ the calculated value (using the bulk dielectric function, Palick[58]) is changed from 1128 to 1033 nm by increasing the number of dipoles from 74 085 to 394 848 as compared to the experimental $\lambda_{max}$ of 1060 nm. An improvement in agreement with experiment is further demonstrated using the JC dielectric function,[57] resulting in a value of 1079 nm, however red-shifted, as expected, due to an increased corresponding difference between the dielectric functions at longer wavelengths. It was shown that roughness and major modifications of the end-cap geometry[59] could cause significant red-shifts. This is not observed in the experimental data we report. The AuNRs we synthesized have the single crystalline structure regardless of $R$ except for the longest AuNR ($R = 14.5$). The facets enclosing the side of Au NRs are {110} and {100} and the growth direction is [001], consistent with previous work.[60]

However, the experimentally determined standard deviations of the characterized geometries can still influence computational results. As further refinements of experimental AuNR synthesis will be carried out, with experimental shape control protocols[21] important for such advances, more precise geometries could be considered computationally, in comparison to predicted structures.[61] This will enable development of computationally derived predictive structure−property relationships that will, in turn, assist in the routine experimental characterization of AuNRs, recently pointed out by Odom et al.[62] It was emphasized that one of the next anticipated advances in tailoring LSPRs is to model structures with desirable optical properties first, followed by synthesis.

Broadening of the LSPR is noted experimentally, which could be due, in part, to a distribution of $R$s in the sample.[63] A number of parameters affect the line-width of the AuNR LSPR. If the particle size is comparable to the mean free path of the conduction electrons in the bulk, the intrinsic width of the dipole plasmon polarization is increased due to scattering from the particle surface,[64] written as $\gamma(L_{eff}) = \gamma_0 + Av_F/L_{eff}$, where the dephasing $\gamma_0$ is due to radiative and nonradiative decay, $A$ is a surface scattering parameter, and $v_F$ the Fermi velocity of the bulk metal. Interestingly, for AuNRs, an increase of $R$ could cause a decrease in the dephasing because of suppression of interband damping.[5] To understand some of these processes, an expansion of the Drude model is often carried out,[65,66] fitted to the JC[57] data. Note that an extension of this model to core−shell structures, as recently carried out by Bruzzone,[67] may not be justified, as in these systems the broadening for the core and the shell may differ from what constitutes individual particles. Indeed, a silver lining on AuNRs causes so-called a "plasmonic focusing", resulting in a narrowing of the ensemble line-width.[63]

Next, we considered the characteristics of AuNR pairs. AuNR ($R = 5.5$) pairs were prepared by the procedure described in the Experimental section. A mixture of unreacted single AuNRs and AuNR pairs resulted, as compared to a solution of single AuNRs only (TEM images in panels a and b of Figure 3, respectively), clearly demonstrate the presence of AuNRs pairs. A blue-shift of the longitudinal LSPR (from 975 to 775 nm for rather broad spectra) and a red-shift of the transverse plasmon (from 512 to 545 nm), were observed experimentally, as shown in Figure 3c, as a function of the inter-rod distance, consistent with previous evaluations.[50,68] Notably, computational $\Delta\lambda$ LSPR shifts for side-by-side AuNRs of corresponding dimensions, as dependent on the inter-rod distance, reproduced the blue-shift and red-shift, respectively, for the longitudinal and transverse LSPRs, respectively (Figure 3d). Indeed, it has been demonstrated[69] that pairs of spherical gold nanoparticles can be used to measure internanoparticle distances due to dependence on the plasmon coupling. Note that possible change of the medium in this case has to be taken into account because of the functionalization, where a larger refractive index would cause a red-shift,[70] as is expanded upon in the next section.

**Au−Ag Core−Shell Nanostructures.** Growth mechanisms, as demonstrated by the evolution of Au−Ag core−shell structures, were previously investigated to possibly explain experimental observations.[16,22,23] To gain an initial understanding of the changes in shape and structure during synthesis of Au−Ag core−shell nanostructures, the optical properties for core−shell spheroids were calculated, as shown in Figure 4a,a−c, based on an Au prolate spheroid geometry with dimensions of ($34 \times 34 \times 82$) nm along $x$, $y$, $z$. Thereafter, accretion was developed at the two ends of the NR along $z$ at an interval of 2 nm (Figure 4a,b), and finally developing an Au−Ag core−shell structure with the Ag coating covering the whole Au interior, becoming thicker at an interval of 1 nm. As the Ag coating grows along the $z$ axis of the Au spheroid (Figure 4a,b), the longitudinal plasmon resonance shifts to longer wavelength, primarily due to an increase in $R$, as expected and discussed above, while as the Ag coating grows in all dimensions, as shown in Figure 4a,c, $\lambda_{max}$ exhibits a blue-shift, primarily because of an overall decrease in $R$ (summarized in Figure 4b). The results for the core−shell structure in Figure 4b represent accretion of Ag all around for the largest $R$ in the Au-tipped structure. The results are consistent with experimental observations that upon increase of the overall amount of deposited Ag, the longitudinal LSPR blue-shifts.[71] Of course, the situation would be reversed if we considered oblate spheroids. The influence of the different composition of an Au−Ag core−shell structure as compared to an Au spheroid will be small due to the similarity in the dielectric functions for the spectral range of interest. A somewhat steeper slope in the LSPR as a function of $R$ for the Au−Ag

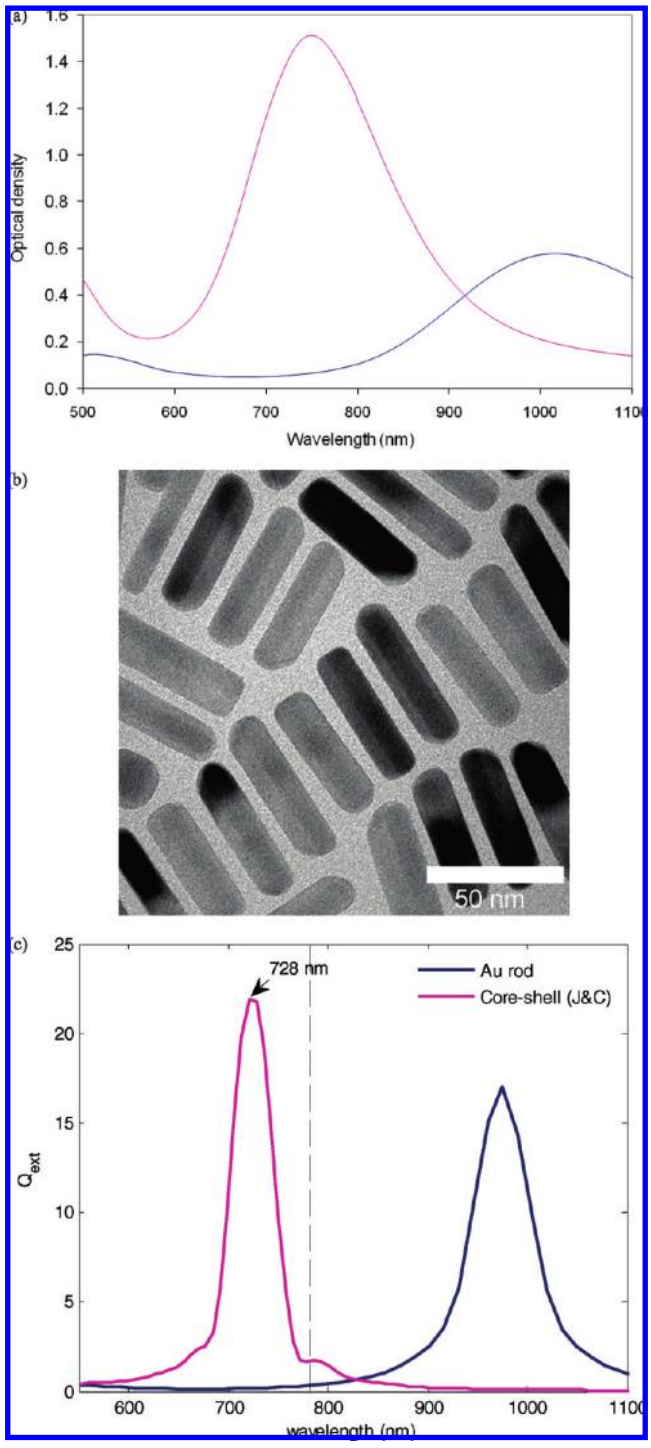


**Figure 6.** (a) Experimental spectra of Au and Au−Ag core−shell NRs of dimensions $L = 50.9 \pm 8.6$ nm; $D = 9.1 \pm 1.5$ nm (blue) and $L = 56.6 \pm 7.1$ nm; $D = 17.4 \pm 3.7$ nm (pink) with (b) corresponding TEM image; (c) calculated spectrum for core−shell Au−Ag structure of $L = 57$ nm, $D = 17$ nm, using a dimension of the inner core of $L = 51$ nm, $D = 9$ nm.

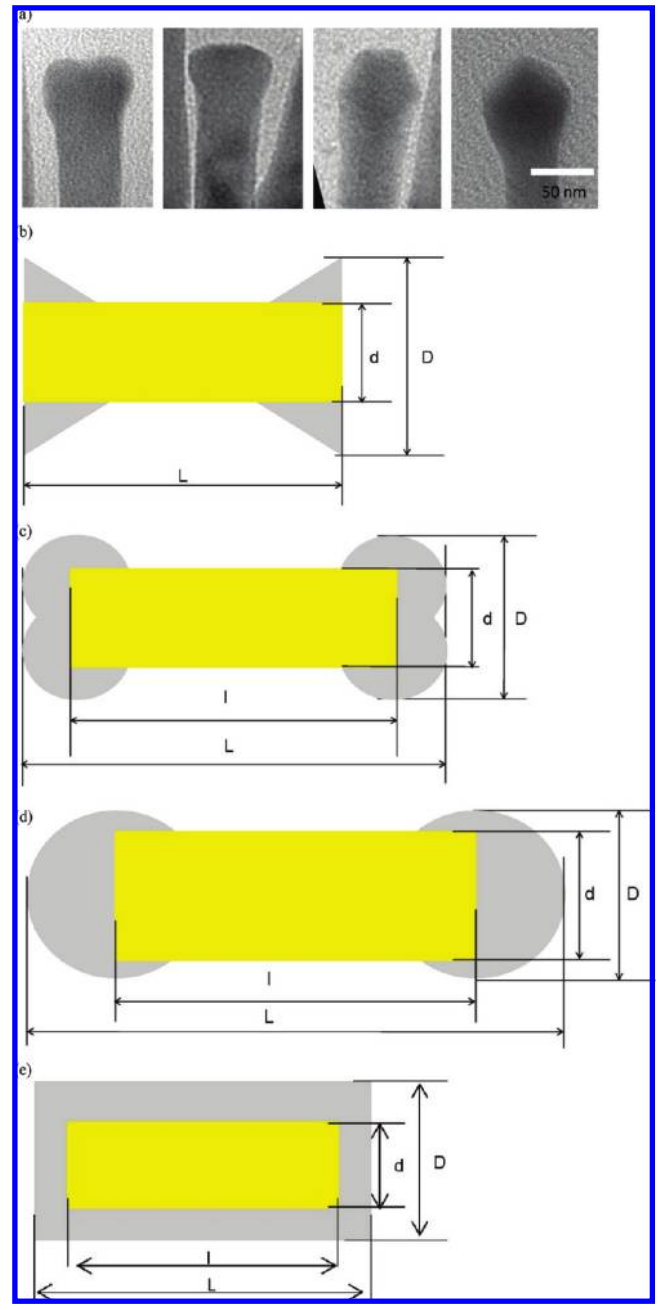


**Figure 7.** Experimental characterization of core−shell NR-like structures (a), as compared to the so-called (b) dogbone1, (c) dogbone2, (e) dumbbell, (e) core−shell structures.

core−shell structure as compared to Au (see Figure 4b) is due to the difference.

Experimentally we demonstrated that for an AuNR of dimension $L = 88.05 \pm 23.00$ nm, $D = 11.24 \pm 1.80$ nm, a blue-shift is observed in the longitudinal LSPR upon increasing the concentration of $AgNO_3$ in synthesizing the Au−Ag core−shell structures (see Figure 5a and Table 1, with the morphology shown in Figure 5b). Specifically, as the thickness of the shell increases from 2 nm for sample 4 to 4.8 nm in sample 6, with a corresponding decrease in $R$, namely, from 6.0 to 3.8, a blue-shift from 925 to 820 nm is observed experimentally (Figure 5a), consistent with the calculated results shown in Figure 4, however, for smaller $R$s and a different NR-like geometry. Once again, the changes are primarily due to a change in geometry for the spectral range examined. In addition, we carried out calculations for AuNRs of $L = 88$ nm, reproducing a blue-shift for $R = 5.8$ relative to $R = 4.2$, from 1082 to 883 nm, attempting to use a geometry consistent with the experimental supposition (Figure 5b). In the core−shell structures, the uncertainty in the overall NR geometry combined with the uncertainty in the amount and heterogeneity of thickness of deposited silver could explain, in part, calculated deviations from the experimental values. The experimentally observed values could also be red-shifted due a somewhat larger refractive index of the environment. To examine the effects of the medium and assess the

**TABLE 2: Geometrical Parameters of the Au−Ag Core−Shell Structures Shown in Figure 7b−d (Dimensions in nm) and the Corresponding Calculated $\lambda_{max}$(nm)**

| | *L* | *D* | *l* | *d* | $\lambda_{max}$ |
|---|---|---|---|---|---|
| Au−Ag dogbone1, Figure 7b | 53 | 26 | 53 | 21 | 700 |
| Au−Ag dogbone2, Figure 7c | 70 | 20 | 40 | 10 | 1100 |
| Au−Ag dumbbell, Figure 7d | 68 | 30 | 40 | 20 | 708 |
| Au−Ag core−shell, Figure 7e | 57 | 22 | 40 | 10 | 676 |

calculations for large NRs, of interest in future work, DDA results for a model core−shell based on that shown in Table 2S (Supporting Information) were carried out, shown to be consistent with previous results[31] for varying *R*s and media refractive indices.

In probing more carefully core−shell Au−Ag NR-like structures (Figure 6), we showed that a better agreement with experiment is obtained (Figure 6c) in using the JC dielectric function. The overall trend for core−shell NR-like structures is consistent with the experimental results of Xiang et al.,[22] where a blue-shift of about 217 nm was observed after 30 min of the start of the reaction to synthesize Au−Ag core−shell NRs, specifically for AuNRs of about $L = 61$ nm, $D = 14$ nm. Interestingly, calculations for an Au−Ag NR core−shell structure previously characterized ($L = 65$ nm, $D = 22$ nm with a core of $L = 61$ nm, $D = 14$ nm),[22] resulted in values of 700 and 710 nm using the Palik and JC dielectric functions, respectively, in comparison with the measured value of 750 nm.[22] The DDA result reported by Xiang et al.[22] was 670 nm.

To further explore the range of engineered bimetallic nanoparticles, this technique could be applied to core−shell NR-like structures, as shown by TEM images in Figure 7a. Figure 7b−e summarizes schematically possible structures, such as so-called dogbone, dumbbell, and related NR geometries, and with the corresponding geometry parameters and calculated $\lambda_{max}$ listed in Table 2. The red-shift in the dogbone structure is consistent with previous work,[71] in which it has been pointed out that for core−shell structures an interplay between a decrease in *R* (which blue-shifts the peak, as discussed above), and the development of dogbone or dumbbell-like lobes which red-shifts the longitudinal peak due to increased *R*, has to be taken into account. Indeed, the silver accretion that develops in the lobes of the AuNR dogbone2 (Figure 7c) as compared to dogbone1 (Figure 7b), increases *R*, causing a red-shift of the LSPR from 700 to 1100 nm. Once again, note that the dominant contribution results from changing *R*, as the materials' dielectric responses are similar in the spectral range of interest. Only a small difference is observed between the dogbone1 and a dumbbell corresponding geometry with a similar *R*. The Au−Ag core−shell structure of Figure 7e resulted in a resonance maximum at 676 nm, in agreement with the experimentally reported values.[53] Of course, experimental conditions in synthesizing these complex core−shell nanostructures can cause changes in the geometry.

Overall, the experimental control achieved in our work in secondary growth, such as that shown in Figure 7a, could enable future development of nano architectures for applications that require plasmon response tunability. For example, recently, bioconjugated AuNRs and silver nanoparticles were used in TEM imaging of pancreatic cancer cells.[72]

## Conclusion

In combining synthesis of Au and Au−Ag core−shell NR-like structures of high purity and for a broad range of *R*s with theoretical prediction, experimentally observed trends of the LSPRs could be explained, while at the same time calculated structure−property relations emerged more clearly. Specifically, the linear relationship between the longitudinal LSPR and the AuNR aspect ratio was validated up to an aspect ratio of about 15, in good agreement with the experimentally measured values for the high-purity solutions of AuNRs. Deviations could be explained by inaccurate geometric characterization or possible effects of the environment. Further investigation with more accurate geometrical parameters will be carried out in future work, because it is the approach of computation for well-characterized nanostructures, as presented in this work, which would enable derivation of structure−property relations for routine use in experimental characterization. In addition, effects of the AuNR morphology were studied for AuNR pairs, emphasizing the importance of well-controlled synthesis and characterization for development of prediction-based relationships. Larger NR-like structure are also of interest, e.g., as recently synthesized and characterized,[73] requiring further theoretical analysis for higher-order LSPRs.[74]

In aiming to engineer complex core−shell nanostructures, we investigated changes in the LSPR upon growth of the NR-like materials, showing qualitative agreement with experiment. In future work, LSPRs of nanostructures of increased complexity and composition by shape-controlled synthesis,[75] systematically and under the same experimental conditions, will be further analyzed in comparison to computational results based on hypothesized geometries. For example, most recently, NR-shaped gold nanorattles were synthesized, showing improved sensitivity of the plasmon resonance to changes in the dielectric environment,[76] while complex nanostructures, for example, Ni-coated Pt tip-coated AuNRs, leading to nanoparticles that can be aligned under an external magnetic field,[77] and Pt−Ag alloy nanoislands on AuNRs were fabricated for improved catalytic activity.[78]

**Acknowledgment.** The authors thank the referees for excellent comments. The DoD High Performance Computing Modernization Program is gratefully acknowledged for computer time and the AFRL DoD Supercomputer Resource Center for helpful support.

**Supporting Information Available:** DDA calculations of longitudinal and transverse $\lambda_{max}$ (nm) for AuNRs of different aspect ratios, as well as for a model core−shell with varying aspect ratios and refractive indices of the medium. This material is available free of charge via the Internet at http://pubs.acs.org.

## References and Notes

(1) Huang, X.; El-Sayed, I. H.; Qian, W.; El-Sayed, M. A. *Nano Lett.* **2007**, *7*, 1591.

(2) Kreibig, U.; Vollmer, M. *Optical Properties of Metal Clusters*; Springer: Berlin, 1995. Maier, A. A.; Atwater, H. A. *J. Appl. Phys.* 2005, *98*, 1011101.

(3) Ghosh, S. K.; Pal, T. *Chem. Rev.* **2007**, *107*, 4797.

(4) Murphy, C. J.; Gole, A. M.; Hunyadi, S. E.; Stone, J. W.; Sisco, P. N.; Alkilany, A.; Kinard, B. E.; Hankins, P. *Chem. Comm.* **2008**, 544.

(5) Soennichsen, C.; Franzl, T.; Wilk, T.; von Plessen, G.; Feldmann, J.; Wilson, O.; Mulvaney, P. *Phys. Rev. Lett.* **2008**, *88*, 077402.

(6) Bryant, G. W.; de Abajo, F. J. G.; Aizpurua, J. *Nano Lett.* **2008**, *8*, 631.

(7) Bakker, R. M.; Yuan, H.-K.; Liu, Z.; Drachev, V. P.; Kildishev, A. V.; Shalaev, V. M.; Pedersen, R. H.; Gresillon, S.; Boltasseva, A. *App. Phys. Lett.* **2008**, *92*, 043101.

(8) Sarychev, A. K.; Drachev, V. P.; Yuan, H.-K.; Podolskiy, V. A.; Shalaev, V. M. *Proc. SPIE* **2003**, *5219*, 92.

(9) Ni, W.; Yang, Z.; Chen, H.; Li, L.; Wang, J. *J. Am. Chem. Soc.* **2008**, *130*, 6692.

(10) Pearce, M. E.; Melanko, J. B.; Salem, A. K. *Pharm. Res.* **2007**, *24*, 2335.
(11) Huang, Y.-F.; Chang, H.-T.; Tan, W. *Anal. Chem.* **2008**, *80*, 567.
(12) Huang, Y.-F.; Lin, Y.-W.; Chang, H.-T. *Langmuir* **2007**, *23*, 12777.
(13) Nakashima, H.; Furukawa, K.; Kashimura, Y.; Torimitsu, K. *Langmuir* **2008**, *24*, 5654.
(14) Sreeprasad, T. S.; Samal, A. K.; Pradeep, T. *Langmuir* **2008**, *24*, 4589.
(15) Smith, D. K.; Korgel, B. A. *Langmuir* **2008**, *24*, 644.
(16) Keul, H. A.; Moller, M.; Bockstaller, M. R. *Langmuir* **2007**, *23*, 10307.
(17) Orendorff, C. J.; Gearheart, L.; Jana, N. R.; Murphy, C. J. *Phys. Chem. Chem. Phys.* **2006**, *8*, 165.
(18) Yang, Z.; Chang, H.-T. *Nanotechnology* **2006**, *17*, 2304.
(19) Yang, Y.; Shi, J.; Kawamura, G.; Nogami, M. *Scripta Mater.* **2008**, *58*, 862.
(20) Liu, M.; Pelton, M.; Scherer, N. F.; Guyot-Sionnest, P. *Proc. SPIE* **2007**, *6471*, n/a.
(21) Grzelczak, M.; Perez-Juste, J.; Mulvaney, P.; Liz-Marzan, L. M. *Chem. Soc. Rev.* **2008**, *37*, 1783.
(22) Xiang, Y.; Wu, X.; Liu, D.; Li, Z.; Chu, W.; Feng, L.; Zhang, K.; Zhou, W.; Xie, S. *Langmuir* **2008**, *24*, 3465.
(23) Park, K.; Vaia., R. A. *Adv. Mater.* **2008**, *20*, 3882.
(24) Sharma, J.; Imae, T. J. *Nanosci. Nanotechnol.* **2009**, *9*, 19.
(25) Taflove, A.; Hagness, S. C. *Computational Electrodynamics: The Finite-Difference Time-Domain Method*; Artech House: Boston, 2005.
(26) De Abajo, J. F.; Garcia, H. A. *Phys. Rev. Lett.* **1998**, *80*, 5180.
(27) Kelly, K. L.; Lazarides, A. A.; Schatz, G. C. *Comput. Sci. Eng.* **2001**, *3*, 67.
(28) Kelly, K. L.; Coronado, E.; Zhao, L. L.; Schatz, G. C. *J. Phys. Chem. B* **2003**, *107*, 668.
(29) Lee, K.-S.; El-Sayed, M. A. *J. Phys. Chem. B* **2006**, *110*, 19220.
(30) Burda, C.; Chen, X.; Narayanan, R.; El-Sayed, M. A. *Chem. Rev.* **2005**, *105*, 1025.
(31) Noguez, C. *J. Phys. Chem. C* **2007**, *111*, 3806.
(32) Gonzalez, A. L.; Reyes-Esqueda, J. A.; Noguez, C. *J. Phys. Chem. C* **2008**, *112*, 7356.
(33) Yang, P.; Portales, H.; Pileni, M.-P. *J. Phys. Chem.* ACS ASAP.
(34) Ungureanu, C.; Rayavarapu, R. G.; Manohar, S.; van Leeuwen, T. G. *J. Appl. Phys.* **2009**, *105*, 102032/1.
(35) Tam, F.; Goodrich, G. P.; Johnson, B. R.; Halas, N. J. *Nano Lett.* **2007**, *7*, 496.
(36) Draine, B. T.; Flatau, P. J. 2003, User Guide to the Discrete Dipole Approximation Code DDSCAT.6.0, http://arxiv.org/abs/astro-ph/0300969.
(37) Purcell, E. M.; Pennypaker, C. R. *Astrophys. J.* **1973**, *186*, 705.
(38) Draine, B. T.; Goodman, J. J. *Astrophys. J.* **1993**, *405*, 685. Draine, B. T.; Flatau, P. J. *J. Opt. Soc. Am. A.* **1994**, *11*, 1491. Draine, B. T. *Light Scattering by Nonspherical Particles: Theory, Measurements, and Geophysical Applications*; Academic Press: New York, 2000, and references therein.
(39) Yurkin, M. A.; Hoekstra, A. G. *J. Quant. Spectrosc. RA* **2007**, *106*, 558.
(40) Penttila, A.; Zubko, E.; Lumme, K.; Muinonen, K.; Yurkin, M. A.; Draine, B.; Rahola, J.; Hoekstra, A. G.; Shkuratov, Y. *J. Quant. Spectrosc. RA* **2007**, *106*, 417.
(41) Bae, E.; Hirleman, E. D. *J. Quant. Spectrosc. RA* **2007**, *107*, 470.
(42) Liu, M.; Guyot-Sionnest, P. *Phys. Rev. B.* **2007**, *76*, 235428.
(43) Myroshnychenko, V.; Rodriguez-Fernandez, J.; Pastoriza-Santos, I.; Funston, A. M.; Novo, C.; Mulvaney, P.; Liz-Marzan, L. M.; Garcia de Abajo, F. J. *Chem. Soc. Rev.* **2008**, *37*, 1792.
(44) NIST Disclaimer: In no case does such identification imply recommendation or endorsement by National Institute of Standards and Technology, nor does it imply that the products are necessarily the best available for the purpose.
(45) Nikoobakht, B.; El-Sayed, M. A. *Chem. Mater.* **2003**, *15*, 1957.
(46) Sharma, V.; Park, K.; Srinivasarao, M. *Proc. Natl. Acad. Sci. U.S.A.* **2009**, *106*, 4981.
(47) Jadzinsky, P. D.; Calero, G.; Ackerson, C. J.; Bushnell, D. A.; Kornberg, R. D. *Science* **2007**, *318*, 430.
(48) Jain, P. K.; Eustis, S.; El-Sayed, M. A. *J. Phys. Chem. B* **2006**, *110*, 18243.
(49) Khlebtsov, B. N.; Khlebtsov, N. G. *J. Phys. Chem. C* **2007**, *111*, 11516.
(50) Lee, K. S.; El-Sayed, M. A. *J. Phys. Chem. B* **2005**, *109*, 20331.
(51) Liz-Marzan, L. M. *Langmuir* **2006**, *22*, 32.
(52) Link, S.; Mohamed, M. B.; El-Sayed, M. A. *J. Phys. Chem. B* **1999**, *103*, 3073.
(53) Liu, M.; Guyot-Sionnest, P. *J. Phys. Chem. B* **2004**, *108*, 5882.
(54) Ah, C. S.; Hong, S. D.; Jang, D. J. *J. Phys. Chem. B* **2001**, *105*, 7871.
(55) Gole, A.; Murphy, C. J. *Chem. Mater.* **2004**, *16* (19), 3633–3640.
(56) For example, see NIST-NCL Protocols, http://ncl.cancer.gov/working_assay-cascade.asp.
(57) Johnson, P. B.; Christy, R. W. *Phys. Rev. B* **1972**, *6*, 4370.
(58) Palik, E. D. *Handbook of Optical Constants of Solids*; Academic: New York, 1985.
(59) Pecharroman, C.; Perez-Juste, J.; Mata-Osoro, G.; Liz-Marzan, L. M.; Mulvaney, P. *Phys. Rev. B* **2008**, *77*, 035418.
(60) Wang, Z. L.; Mohamed, M. B.; Link, S.; El-Sayed, M. A. *Surf. Sci.* **1999**, *440*, L809.
(61) Barnard, A. S.; Curtiss, L. A. *J. Mater. Chem.* **2007**, *17*, 3315.
(62) Odom, T. W.; Nehl, C. L. *ACS Nano* **2008**, *2*, 612.
(63) Becker, J.; Zins, I.; Jakab, A.; Khalavka, Y.; Schubert, O.; Soennichsen, C. *Nano Lett.* **2008**, *8*, 1719.
(64) Moskovits, M.; Srnova-Sloufova, I.; Vlckova, B. *J. Chem. Phys.* **2002**, *116*, 10435.
(65) Hao, F.; Nordlander, P. *Chem. Phys. Lett.* **2007**, *446*, 115.
(66) Drachev, V. P.; Chettiar, U. K.; Kildishev, A. V.; Yuan, H.-K.; Cai, W.; Shalaev, V. M. *Opt. Express* **2008**, *16*, 1186.
(67) Bruzzone, S.; Malvaldi, M.; Arrighini, G. P.; Guidotti, C. *J. Phys. Chem. B* **2006**, *110*, 11050.
(68) Jain, P. K.; Huang, W.; El-Sayed, M. A. *Nano Lett.* **2007**, *7*, 2080.
(69) Reinhardt, B. M.; Siu, M.; Agarwal, H.; Alivisatos, A. P.; Liphardt, J. *Nano Lett.* **2005**, *5*, 2246.
(70) Link, S.; El-Sayed, M. A.; Mohamed, M. B. *J. Phys. Chem. B* **2005**, *109*, 10531.
(71) Liu, J.; Cankurtaran, B.; Wieczorek, L.; Ford, M. J.; Cortie, M. *Adv. Funct. Mater.* **2006**, *16*, 1457.
(72) Hu, R.; Yong, K.-T.; Roy, I.; Ding, H.; He, S.; Prasad, P. N. *J. Phys. Chem. C* **2009**, *113*, 2676.
(73) Kim, S.; Kim, S. K.; Park, S. *J. Am. Chem. Soc.* **2009**, *131*, 8380.
(74) Encina, E. R.; Perassi, E. M.; Coronado, E. A. *J. Phys. Chem. A* **2009**, *113*, 4489.
(75) Xia, Y.; Xiong, Y.; Lim, B.; Skrabalak, S. E. *Angew. Chem.* **2009**, *48*, 60.
(76) Khalavka, Y.; Becker, J.; Soennichsen, C. *J. Am. Chem. Soc.* **2009**, *131*, 1871.
(77) Grzelczak, M.; Rodriguez-Gonzalez, B.; Perez-Juste, J.; Liz-Marzan, L. M. *Adv. Mater.* **2007**, *19*, 2262.
(78) He, W.; Wu, X.; Liu, J.; Zhang, K.; Chu, W.; Feng, L.; Hu, X.; Zhou, W.; Xie, S. *J. Phys. Chem. C* **2009**, *113*, 10505.

JP902448F